Size-dependent attraction of Cu solutes to clusters formed at Ag grain boundaries

Pavel Nikitin [*] and Frederic Sansoz [†]
Department of Mechanical Engineering, The University of Vermont, Burlington, Vermont, USA

(Received 31 May 2025; accepted 27 August 2025; published 15 September 2025)

We report a size-dependent solute clustering mechanism at grain boundaries in a sputtered ultrafine-grained Ag-Cu alloy, where large Cu clusters form despite weak individual solute-solute interactions. X-ray diffraction confirms limited Cu solubility in the Ag matrix, while scanning transmission electron microscopy reveals Cu clustering at both ordinary GBs and GB junctions. Density functional theory calculations show that 12-atom Cu clusters are energetically preferred, while smaller three-atom clusters are significantly less stable. Additional calculations demonstrate a marked increase in solute-cluster attraction energy with cluster size. These findings point to a previously unrecognized pathway for grain-boundary solute clustering in immiscible systems, driven by collective solute-cluster interactions, with implications for segregation behavior and stability in nanocrystalline and ultrafine-grained alloys.

DOI: 10.1103/t7qb-g8n6

I. INTRODUCTION

Solute segregation to grain boundaries (GBs) is a well-established strategy for stabilizing nanocrystalline and ultrafine-grained alloys. By reducing excess GB energy and restricting GB motion, segregation helps preserve microstructural stability under thermal or mechanical stress [1–10]. Prior studies at Sandia National Laboratories have provided direct evidence of heterogeneous solute segregation and clustering at GBs in nanocrystalline Pt-Au alloys [11–14]. Similar solute clustering behavior has also been reported in nanocrystalline Ni-P [15,16], Fe-Cr [17], Ag-Ni alloys [18–20], and in ultrafine-grained Al-Mg alloy [21]. These nanoscale solute clusters at GBs have been linked to improved mechanical and physical properties, including enhanced dislocation hardening [22], superior high-temperature creep resistance [23,24], increased wear resistance [25], and improved electrical conductivity [26–28].

Two primary mechanisms have been proposed to explain solute clustering at GBs: thermodynamic driving forces such as phase separation and nucleation [29], and structural effects like solute trapping at GB junctions [14]. These mechanisms typically require either strong solute-solute attraction or high immiscibility between alloying elements (i.e., a positive heat of mixing). In the Ag-Cu system, however, theoretical predictions suggest weak Cu-Cu interactions at GB, making such clustering unexpected [18,30,31]. In this study, we report experimental evidence of large Cu clusters forming at both ordinary GBs and GB junctions in an ultrafine-grained Ag-Cu alloy produced by magnetron sputtering. Complementary DFT simulations reveal that solute-cluster attraction becomes increasingly favorable as cluster size increases, suggesting a new mechanism in which size-dependent interactions drive the formation of large Cu clusters at GBs, even in systems with weak intrinsic solute-solute attraction.

[*]Contact author: pavel.nikitin@uvm.edu
[†]Contact author: frederic.sansoz@uvm.edu

II. METHODOLOGY

A. Materials synthesis

To produce the Ag-Cu alloy, we utilized DC magnetron co-sputtering. The sputter coater (DST3-T, Element PI) was equipped with Ag (99.99% purity) and Cu (99.999% purity) targets, and a B-doped ⟨100⟩ oriented 4-inch Si wafer was used as a substrate. The distance between the targets and the substrate was 8 cm. Before sputtering, the chamber was evacuated to a base pressure of approximately 5×10^{-4} Pa. Then, ultrahigh-purity argon (99.999%) was introduced into the chamber at a flow rate of 40 standard cubic centimeters per minute (SCCM) to maintain a chamber pressure of 1.6 Pa. The power supplied to the Ag and Cu targets was independently controlled by two power units and set to 200 W and 17 W, respectively. To ensure uniform distribution of Ag and Cu across the substrate, it was rotated at 15 revolutions per minute (RPM). No substrate cooling was enforced during the deposition. The deposition time was 40 min.

B. Materials characterization

The surface microstructure, elemental composition, grain size, and crystallographic orientation of the alloy were characterized using a field-emission scanning electron microscope (FESEM, Zeiss VP300) equipped with X-ray energy-dispersive spectrometry (EDS, Oxford Instruments) and electron backscatter diffraction (EBSD, Oxford Instrument). The Cu atomic percentage was measured by FESEM-EDS for which the error was estimated to be ±0.2 at.%. The crystal structure of the alloy was studied by X-ray diffraction (XRD) using a Rigaku Miniflex II diffractometer with Cu-K radiation, a step size of 0.02°, and a scanning speed of 1°/min. The phase composition was determined using PDF4 (Powder Diffraction File) database. According to Vegard's law [32], the fraction of Cu dissolved in the Ag matrix as a solid solution was estimated from the (111) peak shift relative to the reference Ag XRD pattern. A ThermoFisher Scientific Helios 5CX Dual-Beam (SEM-focus-ion

 ©2025 American Physical Society

beam) microscope was used to fabricate planar specimens for scanning transmission electron microscopy (STEM). STEM analysis was performed using a ThermoFisher Scientific Talos F200i STEM, equipped with a Dual-X EDS system, at the Electron Microscope Facility of Dartmouth College (Hanover, New Hampshire, USA).

C. First-principles calculations

Density-functional theory (DFT) calculations of the energy of relaxed atomic structures were performed using the Vienna ab initio simulation package (VASP) [33]. We used projector augmented wave (PAW) pseudopotentials and the exchange-correlation functional via the gradient generalized approximation in the parametrization of Perdew-Burke-Ernzerhof (PBE) [34]. Due to the large simulation cell, Γ-only mesh was used to sample the Brillouin zone. A plane wave basis set was used to expand the Kohn-Sham orbitals [35] with an energy cutoff of 350 eV. The energy convergence criterion was set to 10^{-5} eV. Geometry optimization was considered converged when the residual forces on each atom were less than 10^{-2} eV/Å. All DFT calculations have been performed on the supercomputer Perlmutter at the National Energy Research Scientific Computing Center (NERSC).

The segregation energy (ΔE_{seg}) for each GB atom site was calculated as the substitutional energy difference between the bicrystal described in Sec. III C 1 and a perfect crystal of identical size as:

$$\Delta E_{seg} = \left(E^{pure}_{GB} - E^{solute}_{GB}\right) - \left(E^{pure}_{crystal} - E^{solute}_{crystal}\right) \quad (1)$$

Specifically, the substitutional energy at a GB site was obtained as the total energy difference between a pure GB (E^{pure}_{GB}) and a GB structure where a single Ag atom was replaced by a Cu atom at that site (E^{solute}_{GB}). Similarly, the substitutional energy in the perfect crystal was calculated as the energy difference between the pure single crystal ($E^{pure}_{crystal}$) and the same structure with one Ag atom substituted by a Cu atom ($E^{solute}_{crystal}$).

III. RESULTS

A. Microstructure and phase composition of sputtered Ag-Cu alloy

The surface microstructure and grain texture of a 4.5 μm-thick Ag-4.9 at.% Cu alloy sputtered on an Si substrate are presented in Figs. 1(a) and 1(b), respectively. As shown in Fig. 1(b), the sputtered Ag-Cu alloy had a grain size of 160 ± 70 nm. Many grains showed a strong ⟨111⟩ texture, which is typical for magnetron sputtered Ag [36].

The XRD spectrum of the alloy [Fig. 1(c)] featured a main (111) peak at 38.28° and (200), (220), (311), and (222) side peaks. All peaks matched those of the reference FCC Ag but were shifted to higher diffraction angles (θ), with the main (111) peak notably shifted from 38.12° to 38.28°. According to Bragg's law, an increase in θ corresponds to a decrease in the interplanar lattice spacing from either substitutional Cu atoms or film stresses induced by magnetron sputtering [37–39]. To subtract the potential contributions of stresses on lattice spacing measurements, we additionally performed XRD on a pure Ag film deposited on a Si substrate under the same sputtering conditions as the Ag-Cu alloy. We found the lattice constant of the pure Ag film and Ag-4.9% Cu film to be $a_{Ag} = 4.079457$ Å and $a_{Alloy} = 4.069198$ Å, respectively. The Vegard's law gives an estimate of the fraction of Cu atoms dissolved into the crystalline Ag matrix as:

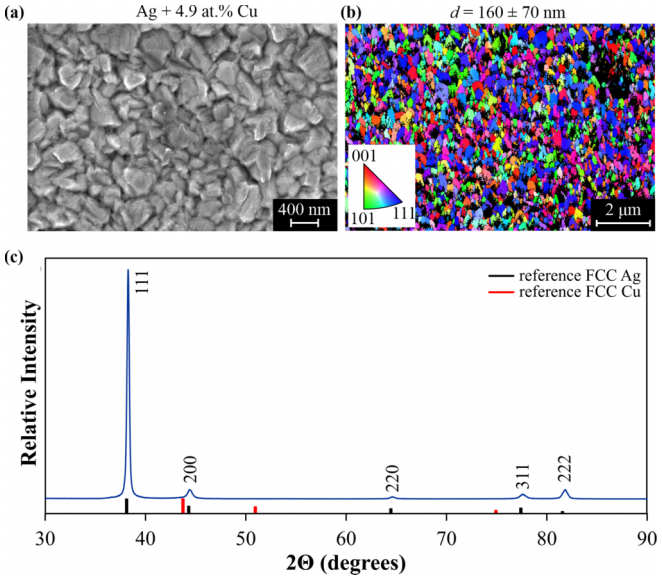

FIG. 1. Microstructure of a sputtered Ag-4.9% Cu alloy on Si substrate. (a) FESEM micrograph and (b) EBSD orientation map of the top surface. (c) XRD spectrum.

$$X_{Cu} = \left(a_{Alloy} - a_{Ag}\right)/\left(a_{Cu} - a_{Ag}\right) \quad (2)$$

Using $a_{Cu} = 3.615$ Å for FCC Cu, Eq. (1) reveals that only 2.21% of Cu atoms were dissolved in the crystalline Ag phase. This value is lower than the overall Cu concentration of 4.9 at. %, suggesting that the excess Cu was segregated to GBs.

B. Solute segregation and clustering characterized by STEM

Figure 2 shows STEM results from the magnetron-sputtered Ag-Cu alloy. As can be seen from this figure, Cu actively segregated to ordinary GBs and GB junctions within the Ag polycrystal. The distribution of Cu is inhomogeneous

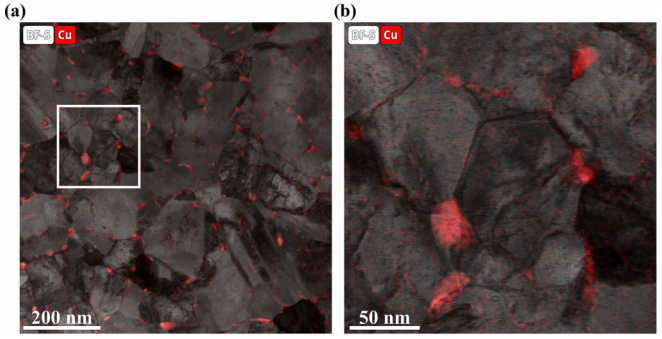

FIG. 2. Grain-boundary solute clustering in the sputtered Ag-4.9% Cu alloy. (a) Mixed bright-field (BF-S) STEM and EDX Cu elemental map characterization; (b) Close-up view of GB network with Cu clusters. All STEM images were obtained from a slice parallel to the film plane near the film center.

and discontinuous across the entire GB network. This segregation behavior is characterized by uneven solute concentrations across different GB interfaces, as well as the formation of Cu-rich solute clusters at GBs and GB junctions, as shown in Figs. 2(a)–2(b). Notably, high-resolution STEM images of solute clusters [Fig. 2(b)] show a wide range of cluster sizes, varying from large and medium-sized clusters at some GB triple junctions but no cluster at other junction. Some small clusters in Fig. 2(b) can be found in single GBs farther away from large clusters at GB junctions. These findings strongly suggest that different thermodynamics forces drive the growth of Cu solute clusters at GBs in the sputtered Ag-Cu alloy.

It should be noted that the substrate was not actively cooled during magnetron sputtering, resulting in heating that can be considered an annealing process. Although our setup did not allow for direct thermocouple measurements during deposition, the substrate temperature, measured with a pyrometer 5 min after shutting down the system and opening the chamber, was approximately 60° C. At the same time, Shapovalov *et al.* reported that the substrate temperature can reach 70° C during 400 W DC magnetron sputtering of Cu target [40], which is consistent with our measurement. Taken together, these observations allow us to conservatively estimate that the substrate temperature during deposition was within the range of 60−100° C. In other words, the deposited material experienced low-temperature annealing and can be considered partially equilibrated.

This STEM study highlights key differences from previous MD simulation results. MD studies on FCC Ag bicrystals consistently reported only weak attraction between Cu solutes segregated to GBs, largely due to the use of interatomic potentials not calibrated for GB segregation or solute interactions [19].

In Ag polycrystals [18,30,41], MD simulations predicted a uniform distribution of Cu solutes at GBs with no clustering observed at the boundaries or their junctions for Cu concentrations below 6 at. %. At higher concentrations, only short-range ordering in the form of three-atom Cu clusters was observed.

In contrast, our STEM results in the sputtered Ag-4.9 at. % Cu alloy show the formation of significantly larger Cu clusters at GBs, contradicting all previous MD findings for Ag-Cu alloys. We attribute this discrepancy to the influence of solute cluster size on solute-solute attraction. This effect was recently proposed in an atomistic simulation by Nenninger and Sansoz [41] to explain size differences between solute clusters forming at different GB junctions in Ag-Ni alloys. However, this size-dependent attraction has not been fundamentally investigated. The following section uses DFT to explore this hypothesis.

C. Size-dependent solute attraction studied by DFT

1. GB segregation energy

DFT was used to calculate the segregation energy of a single Cu solute into different GB sites of a Σ9 (221) symmetric tilt bicrystal with a ⟨110⟩ tilt axis. The simulation cell had dimensions of 17.65 × 49.92 × 17.65 Å^3 in the x, y, and z directions, respectively, and consisted of 18 (221) layers and 864 atoms in total, as shown in Fig. 3(a). A vacuum layer of 10 Å was added in the y-direction to ensure adequate convergence, following the approach described in [19] [Fig. 3(a)]. This GB consisted of a periodic arrangement of E structural units with four distinct GB segregation sites, as shown in Fig. 3(b). This type of interface is representative of a GB with high energy due to its high GB excess free volume [42]. In Fig. 3(c), DFT shows that a Cu solute is strongly attracted to Sites 1 and 2, i.e., these sites have negative segregation energies, whereas Sites 3 and 4 exhibit an anti-segregation behavior (positive segregation energies).

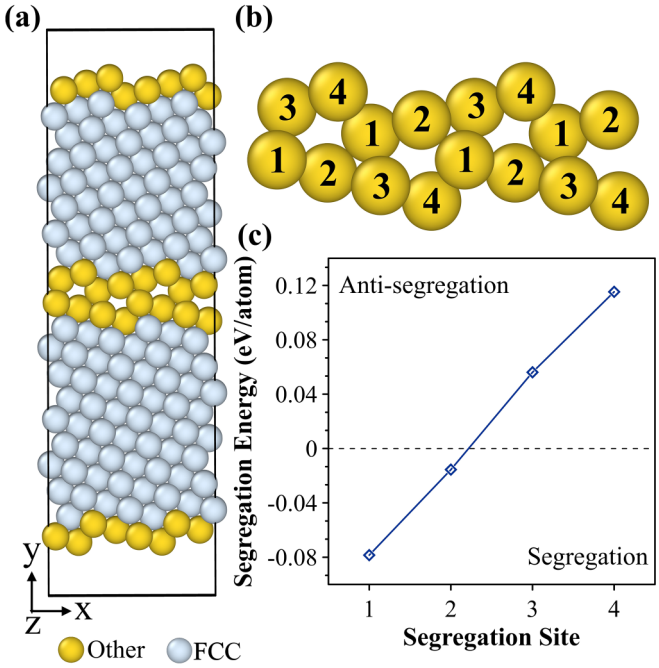

FIG. 3. DFT calculation of Cu segregation energies in a Σ9 (221) symmetric tilt GB. (a) Bicrystal atomic model (bottom grain has X = [11$\bar{4}$], Y = [221], Z = [1$\bar{1}$0] and top grain has X = [11$\bar{4}$], Y = [$\bar{2}\bar{2}\bar{1}$] and Z = [$\bar{1}$10]). (b) Four segregation sites in the GB interface. (c) Cu segregation energy at these sites (negative value indicates segregation).

2. Solute dipole formation energy

In dilute alloys, Wagih and Schuh [43] proposed that Cu solutes occupy only specific GB atom sites with the highest GB segregation energies, leaving majority of GB sites unoccupied. However, when GB segregation exceeds the dilute limit, Cu atoms are forced to occupy less energetically favorable sites. To model this scenario, we considered two Cu atoms: the first occupies the most favorable GB site (e.g. Site 1), while the second is placed at a less favorable but still segregating site (Site 2). The second atom can either occupy a neighboring site, forming a bonded dipole [Fig. 4(b)], or be positioned farther away to minimize short-range solute-solute interactions [Fig. 4(a)].

We define the formation energy of a GB solute dipole as the total energy difference between these two configurations, where a negative value indicates a preference for bonded dipole formation. As shown in Table I, Cu exhibits a slight tendency to form bonded dipoles, with a formation energy of −0.016 eV. This tendency is relatively weak compared

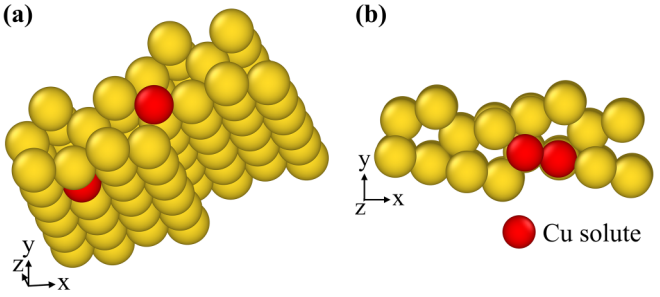

FIG. 4. Solute dipole configurations in a Σ9 (221) symmetric tilt GB bicrystal. (a) Two distant Cu atoms in unbonded configuration and (b) a bonded Cu dipole.

to Ni solutes in the same type of Σ9 (221) Ag GB, where the dipole formation energy is nearly five times greater at −0.077 eV [19].

3. Cluster formation energy

Since two Cu atoms tend to form a bonded dipole, we also examined the formation energy of three-atom Cu clusters, similarly to those predicted at random interfaces in Monte-Carlo/MD simulations of Ag polycrystals with Cu content above 8 at.% [30]. In Fig. 5, we analyzed three configurations involving three GB solute atoms: (a) Three distant Cu atoms each placed at equivalent GB Site 1 positions [Fig. 5(a)] a bonded Cu dipole with a third Cu atom placed distantly at Site 1 [Figs. 5(b)] a fully bonded three-atom cluster represented by three substitutional Cu solutes occupying adjacent Sites 1, 2, and 3 [Fig. 5(c)]. Our DFT calculations (Fig. 5) show that the most energetically favorable configuration is the one with three distant solutes [Fig. 5(a)], with an energy difference relative to the same three atoms in the grain of E∗ = −0.273 eV. In contrast, the three-atom Cu cluster configuration [Fig. 5(c)] is the least energetically favorable. We conclude that solute-solute attraction remains weak in the case of three solute atoms, limiting the formation of small atomic clusters.

Next, we considered a larger, columnar-type cluster composed of 12 solute atoms of Cu. These solute atoms filled four layers of GB sites 1, 2, and 3 [Fig. 6(c)]. For comparison, we also examined configurations with either four separated three-atom Cu clusters [Fig. 6(b)] or 12 Cu atoms randomly distributed in the GB [Fig. 6(a)]. To further minimize the influence of segregation positions, all configurations contained the same number of Cu atoms at Site 1 (the most energetically favorable site for Cu segregation at this type of interface).

First, we established that 12 randomly distributed Cu atoms energetically tend to segregate to the GB rather than remain

TABLE I. Solute dipole formation energy in the Σ9 (221) GB by DFT.

Solute	Dipole formation energy (eV)
Cu	–0.016
Ni [19]	–0.077

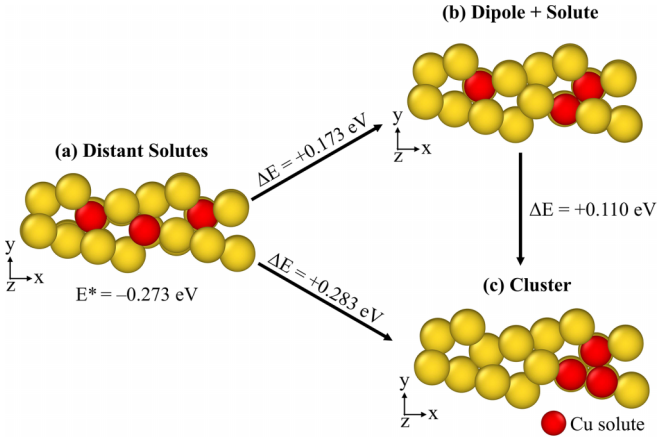

FIG. 5. Energetics of three-atom solute cluster configurations in a Σ9 (221) symmetric tilt GB. (a) Unbonded distant Cu atoms at Site 1. (b) Bonded Cu dipole and a distant Cu solute at Site 1. (c) Fully bonded Cu cluster.

in the interior of the Ag grain, with an energy difference of E∗ = −0.416 eV [Fig. 6(a)]. This configuration was used as a reference for comparison with other atomic arrangements. Among the three tested configurations, the formation of separated three-atom clusters at the GB was found to be the least energetically favorable, with ΔE = +0.242 eV [Fig. 6(b)]. This energy, however, is slightly lower than that of a single three-atom Cu cluster [Fig. 5(c)] for which ΔE = +0.283 eV with respect to 3 randomly spaced Cu atoms [Fig. 5(a)]. This variation suggests a potential influence of long-range solute-cluster interactions.

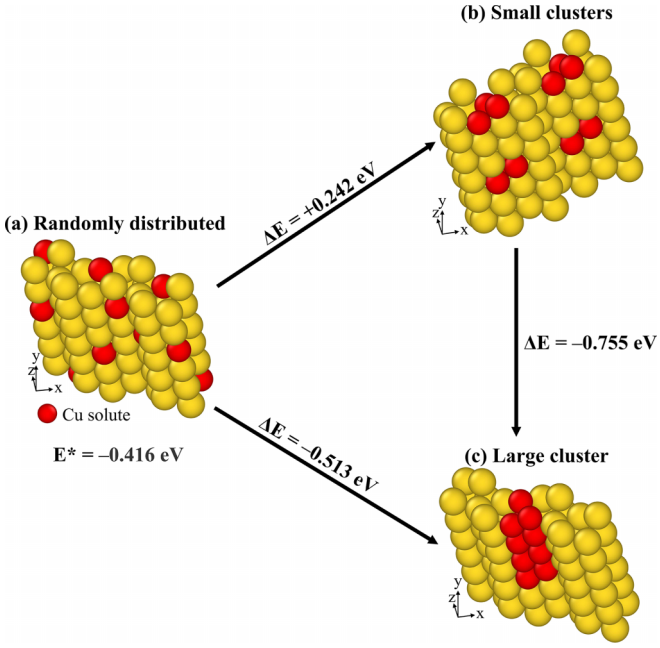

FIG. 6. Energetics of twelve-atom cluster configurations in Σ9 (221) symmetric tilt GBs. (a) Randomly distributed 12 Cu atoms. (b) Four divided three-atom bonded clusters. (c) One large, columnar-type bonded cluster.

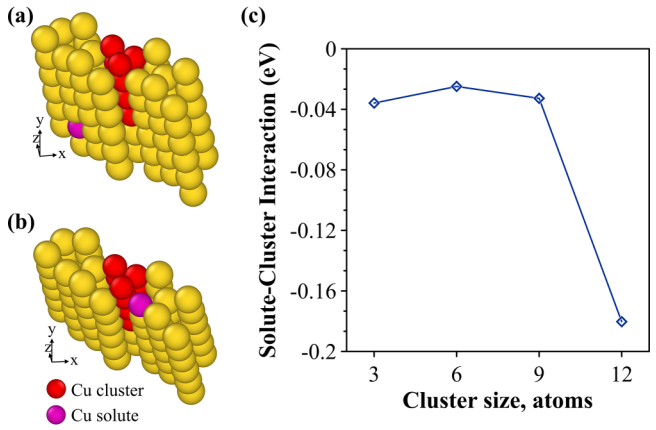

FIG. 7. Cluster size effect on solute-cluster attraction in a Σ9 (221) symmetric tilt GB. (a) Distant solute-cluster and (b) dipole-like solute-cluster configurations. (c) Solute-cluster interaction energy (eV) for different cluster sizes (negative value indicates attraction).

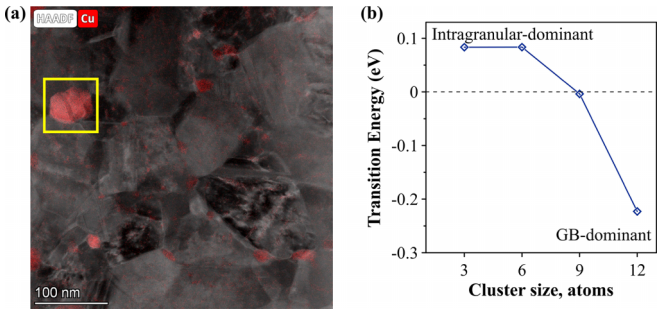

FIG. 8. Precipitate formation in Ag-Cu alloys. (a) Mixed High Angle Annular Dark Field (HAADF) STEM and EDX Cu elemental map characterization of the Ag-4.9 at.% Cu alloy annealed for 6 h at 200° C (yellow square indicates an example of a Cu precipitate); (b) Transition energy from intragranular to intergranular clustering as a function of cluster size, as predicted by DFT.

In contrast, the configuration containing a large bonded Cu cluster [Fig. 6(c)] is the most energetically favorable, indicating strong solute-solute attraction, even for Cu solutes with inherently weak mutual interactions. These results suggest that solute attraction depends on cluster size, which in turn affects the overall segregation behavior at GBs.

4. Size-dependent solute-cluster interaction energy

Past atomistic studies have quantified GB solute-solute interactions by considering the interaction between only two solute atoms [19,31,44]. Instead of evaluating classical solute-solute interactions as in those studies, we investigated solute-cluster interactions, wherein a single solute atom interacts with a pre-formed cluster of varying sizes. Specifically, we considered clusters consisting of 3, 6, 9, and 12 Cu atoms. For each cluster size, we performed two calculations: (i) the solute atom was positioned far away from the cluster to decrease their interaction [Fig. 7(a)] and (ii) the solute atom was placed adjacent to the cluster, forming a dipole-like configuration [Fig. 7(b)]. The solute-cluster interaction energy was defined as the total energy difference between these two configurations, with a negative interaction energy indicating a long-range solute attraction to the pre-formed cluster. To ensure consistency, the solutes in both the adjacent and distant configurations occupied the same GB site. In Fig. 7(c), DFT calculations show that configurations with Cu cluster sizes of 3, 6, and 9 atoms exhibit a slight tendency to attract an additional Cu solute. When the cluster size increases to 12 atoms, the solute-cluster interaction strengthens significantly, dropping to −0.181 eV and indicating a strong attraction between the solute and the cluster.

D. Precipitates vs GB solute clusters

Under equilibrium conditions at room temperature, Ag and Cu exhibit extremely limited mutual solubility of less than 1 at.% [45,46]. To extend this limit, various non-equilibrium processing techniques, including magnetron sputtering, can be utilized [45]. For instance, S. Gohil *et al.* reported that Ag-Cu thin films sputtered at room temperature exhibited Cu solubility as high as 13 at.%, accompanied by the formation of a hexagonal (4H) phase [45]. This high solubility, however, reflects a non-equilibrium state of the alloy. Upon subsequent annealing, the system tends to return toward equilibrium, resulting in phase separation of the α-solid solution (Ag-rich phase) with the formation of the β precipitates (Cu-rich crystals) [47,48]. In particular, for the Ag-8 at.% Cu alloy, Hamana and Boumaza reported the formation of various types of Cu-rich precipitates depending on the temperature of annealing [47]. The thermodynamic aspects of precipitate formation warrant a dedicated investigation and are beyond the scope of this study. Here, our primary goal is to identify the physical boundary between GB segregation and precipitation formation. To this end, we performed additional annealing of the Ag-4.9 at.% Cu specimen for 6 h at 200° C. This temperature, as reported in [47], corresponds to the cells formation at initial GBs and was specifically chosen to further equilibrate the microstructure while preventing complete decomposition of the alloy into separate Ag and Cu phases. Prior to annealing, the specimen was peeled off from the Si substrate and treated as a free-standing foil, thus excluding any possible interaction with Si.

Figure 8(a) shows STEM results from the Ag-4.9 at.% Cu alloy after annealing at 200° C for 6 h. As can be seen from this figure, Cu atoms tend to form Cu-rich clusters, primarily localized at GB junctions. Notably, after annealing, a distinct precipitate with a characteristic shape and a radius of approximately 25 nm can be clearly observed (highlighted with a yellow square in Fig. 8(a), which is consistent with the results reported in Ref. [47]. To gain insight into the early stages of precipitate formation, we modeled small Cu clusters containing 3, 6, 9, or 12 Cu atoms as simplified precursors (nuclei) that may eventually grow into larger precipitates. We aimed to determine which mechanism is energetically preferred at this early stage – intergranular (GB) clustering or intragranular clustering that could later develop into precipitates. To this end, we calculated the transition energy from intragranular to intergranular clustering, defined as the energy difference between Cu clusters located at the GB and those embedded within the Ag grain of the Σ9 (221) symmetric tilt bicrystal [Fig. 8(b)]. The calculated transition energies

TABLE II. Energetic properties of Cu in Ag predicted by DFT and existing interatomic potentials.

Configuration	DFT	Wu-Trinkle	Williams-Mishin-Hamilton	Zhou-Johnson-Wadley
		Segregation energy (eV/atom)		
Site 1	–0.078	–0.299	–0.198	–0.090
Site 2	–0.015	–0.235	–0.083	–0.019
Site 3	0.056	0.049	–0.001	0.043
Site 4	0.115	–0.034	0.001	0.029
		Dipole formation (eV)		
	–0.016	–0.030	–0.058	0.001
		Cluster formation energy (eV)		
3 atoms	0.283	0.558	0.232	0.320
12 atoms	–0.512	0.075	–1.362	–0.156
		Solute-cluster interaction (eV)		
3-atom cluster	–0.034	0.179	–0.027	–0.003
6-atom cluster	–0.025	0.055	–0.079	–0.081
9-atom cluster	–0.034	0.628	–0.047	0.001
12-atom cluster	–0.176	0.376	–0.049	0.009
		Transition energy (eV) from intragranular to intergranular clustering		
3-atom cluster	0.083	–0.318	–0.196	0.025
6-atom cluster	0.083	–1.305	–0.476	–0.069
9-atom cluster	–0.004	–2.250	–0.813	–0.264
12-atom cluster	–0.223	–2.950	–1.186	–0.485

reveal a size-dependent preference between GB clustering and intragranular clustering. The formation of small clusters containing 3 or 6 Cu atoms within the grain interior is energetically favorable (an intragranular-dominant scenario), with positive transition energies of 0.083 eV in both cases [Fig. 8(b)]. However, as the cluster size increases, this trend reverses. For 9-atom clusters, the transition energy becomes slightly negative (–0.004 eV), indicating the onset of a preference for GB clustering. At 12 atoms, the transition energy drops significantly to −0.223 eV, clearly establishing GB clustering as the dominant mechanism at this size [Fig. 8(b)]. Notably, this shift coincides with a pronounced decrease in solute-cluster interaction energy to −0.181 eV for the same 12-atom Cu cluster [Fig. 7(c)], further supporting the strong energetic driving force for Cu atoms to aggregate at GBs rather than form precipitates in the bulk.

E. Evaluation of existing interatomic potentials

In the previous sections, we have discussed a wide range of Cu-related energetics in Ag based on extensive DFT calculations, including segregation, dipole formation, cluster formation, solute-cluster interaction, precipitate formation, and intragranular to intergranular clustering transition energies. The purpose of this section is to critically compare these *ab initio* results with predictions from existing interatomic potentials. Such a comparison is essential because reliable potentials that accurately capture these energetic aspects are crucial for large-scale atomistic simulations, which enable the study of microstructural evolution beyond the limits of DFT. Assessing how well current potentials reproduce our DFT benchmarks helps to identify their strengths and limitations, and guides the development of improved models for simulating Cu segregation, clustering, and precipitation phenomena in Ag-Cu alloys.

Table II summarizes the key energetic properties described above, comparing the DFT values with those predicted in the large-scale atomic/molecular massively parallel simulator LAMMPS (0K energy minimization using the conjugate gradient algorithm) by three embedded-atom-method (EAM) interatomic potentials: (i) Wu-Trinkle potential [49], Williams-Mishin-Hamilton potential [50], and Zhou-Johnson-Wadley potential [51]. The data in Table II reveal notable differences between DFT and various interatomic potentials in describing key thermodynamic properties of Cu in Ag. All potentials qualitatively reproduce the segregation energy trend across GB sites, but the absolute values differ significantly. Here, the Zhou-Johnson-Wadley potential shows values closest to DFT. For dipole formation energy, DFT predicts a weakly negative value (–0.016 eV), reasonably approximated by the Wu-Trinkle and Williams–Mishin–Hamilton potentials. In terms of cluster formation, DFT predicts that 12-atom Cu clusters are energetically favorable (–0.512 eV), a trend reproduced only by the Williams-Mishin-Hamilton potential (–1.362 eV) with even stronger binding, while the Wu-Trinkle and Zhou-Johnson-Wadley potentials fail to capture this stabilization. Solute-cluster interaction energies are again best approximated by the Williams-Mishin-Hamilton potential, though it slightly underestimates the interaction strength. However, none of the tested interatomic potentials can properly predict the energetics associated with the transition from intragranular to intergranular clustering.

Overall, none of the tested interatomic potentials provides a quantitatively accurate and consistent description of the

key energetics associated with segregation, clustering, and precipitation. These discrepancies underscore the need for a more accurate potential tailored to the Ag-Cu system to enable reliable large-scale simulations of these phenomena.

IV. DISCUSSION

A salient finding of this study is the heterogeneous formation of large Cu solute clusters at Ag GBs, despite theoretical predictions of weak Cu-Cu attraction at GBs. Our STEM analysis [Figs. 2 and 8(a)] directly revealed the presence of large Cu clusters at both ordinary GBs and GB junctions in a sputtered Ag-Cu polycrystal with relatively low Cu content. Complementary DFT calculations (Fig. 6) showed that the formation of a large, 12-atom cluster is the most energetically favorable configuration. In contrast, smaller three-atom solute clusters were found to be the least favorable (Fig. 5), indicating a strong dependence of solute-solute interactions on cluster size. Further DFT calculations confirmed that the solute-cluster attraction energy increases with the cluster size, from 3 to 12 solute atoms (Fig. 7).

An important question addressed in this study was to determine whether the observed Cu clusters represent extended segregation or the early stages of precipitation. Considering that even the as-deposited Ag-4.9 at.% Cu alloy experienced low-temperature annealing during deposition due to the lack of substrate cooling, it is likely that some of the Cu clusters observed by STEM (Fig. 2) are, in fact, precipitates. This assumption is further supported by STEM analysis of this alloy after annealing at 200° C for 6 h [Fig. 8(a)], which clearly reveals the formation of Cu precipitates. This behavior is caused by the limited mutual solubility of Ag and Cu and their natural tendency toward phase separation as an equilibrium state [45,46]. At the same time, GBs are well-known as favorable nucleation sites for precipitates, where phase transformations can readily occur, including in the Ag-Cu system [47,48,52,53]. The enhanced growth of precipitates at GB interfaces can be explained by the increased excess free volume [30], which provides favorable conditions for GB diffusion [54]. In particular, this may explain the high concentration of Cu clusters observed at triple junctions [Figs. 2 and 8(a)], which possess higher excess free volume compared to ordinary GBs and Ag grains.

While the detailed mechanisms underlying the formation of precipitates at GBs remain a subject of ongoing investigation, our experimental observations and DFT calculations provide strong evidence that solute clusters at GBs serve as effective nucleation sites for precipitation. The DFT results revealed a strong thermodynamic driving force for Cu segregation to GB sites in Ag bicrystal [Fig. 3(c)]. It was also found that once a GB cluster reaches a critical size, its ability to attract additional Cu solutes significantly increases. As shown in Fig. 7, even a small cluster consisting of three Cu atoms already exhibits a measurable attractive effect on nearby Cu solutes, and this trend intensifies as the cluster grows to 12 atoms. Given that magnetron sputtering proceeds via a bottom-up, layer-by-layer deposition process, the evolution of cluster formation can be interpreted in terms of sequential site occupation. Initially, Cu atoms occupy the most energetically favorable GB sites, which do not immediately lead to cluster formation (Fig. 5). Once these high-energy sites are filled, Cu atoms can more easily form bonded dipoles (Fig. 4) or small clusters. This hypothesis is supported by the atomistic simulations of Sansoz and Ke [30], which showed the formation of three-atom Cu solute clusters within GB networks of Ag polycrystals upon thermal annealing, even when weak solute interactions were predicted by the interatomic potential. In subsequent layers, Cu atoms again occupy energetically favorable GB positions, but the likelihood of them being attracted to pre-existing clusters from earlier layers increases. This leads to a snowball effect, whereby the growing cluster eventually becomes the most energetically favorable site for additional solutes. As a result, solute-cluster interactions begin to dominate segregation behavior at the GB.

This energetic preference strongly implies that the precipitation of Cu does not occur spontaneously and independently within the grain interiors, but rather proceeds through a precursor stage involving solute clustering at GBs. In this mechanism, GB clusters act as effective nucleation sites by lowering the energy barrier for phase separation and providing a locally enriched Cu environment that favors the onset of precipitate growth. This aligns with our experimental observations, where Cu clusters and precipitates are located at GBs and triple junctions [Figs. 2 and 8(a)], consistent with the expected formation of Cu solute clusters at these sites. As additional support for this hypothesis, X. Shuai *et al.* demonstrated the same mechanism of precipitation formation through GB segregation and clustering in Al-Cu alloys using structural phase-field crystal simulations [55]. Their work revealed that interfacial solute clustering is a critical precursor step to GB precipitation [55]. Nevertheless, atomistic simulations with a reliable interatomic potential that captures Cu cluster formation at various temperatures are essential to fully reveal the thermodynamic factors driving precipitation at GBs [56].

V. CONCLUSION

An ultrafine-grained Ag-Cu alloy was synthesized using DC magnetron co-sputtering. XRD analysis confirmed partial Cu solubility in the Ag matrix. Direct STEM observations revealed that the remaining Cu segregates inhomogeneously to GBs, forming large Cu clusters at both ordinary GBs and GB junctions, despite prior theoretical predictions of weak Cu-Cu interactions at GBs. To investigate the origin of these clusters, DFT simulations were conducted and revealed strong Cu-Cu attraction effects within large 12-atom Cu clusters. Additional DFT calculations showed that solute-cluster attraction energy increases with the cluster size, from 3 to 12 solute atoms. Based on these results, a mechanism is proposed for the formation of large Cu clusters at Ag GBs, during sputter deposition, which may further act as precursors for the nucleation of nanoscale precipitates, thus providing a segregation-driven pathway for precipitation in immiscible systems. These findings underscore the importance of size-dependent solute-cluster interactions in governing heterogeneous GB segregation, solute clustering, and the early stages of precipitation in nanocrystalline and ultrafine-grained alloys.

ACKNOWLEDGMENTS

STEM imaging was conducted at Dartmouth College Imaging Center with help from Maxime Guinel de France. The support by the U.S. Department of Energy (DOE) under Grant No. DE-SC0020054 is gratefully acknowledged. All simulations have been performed on the supercomputer Perlmutter at the National Energy Research Scientific Computing Center (NERSC), a U.S. Department of Energy Office of Science User Facility located at Lawrence Berkeley National Laboratory, operated under Contract No. DE-AC02 05CH11231. The Zeiss VP300 instrument used in this study was acquired through the National Science Foundation (NSF) under MRI Grant No. 1828371.

DATA AVAILABILITY

The data that support the findings of this article are not publicly available. The data are available from the authors upon reasonable request.

[1] T. Chookajorn, H. A. Murdoch, and C. A. Schuh, Design of stable nanocrystalline alloys, Science **337**, 951 (2012).

[2] H. A. Murdoch, and C. A. Schuh, Stability of binary nanocrystalline alloys against grain growth and phase separation, Acta Mater. **61**, 2121 (2013).

[3] D. Raabe, M. Herbig, S. Sandlöbes, Y. Li, D. Tytko, M. Kuzmina, D. Ponge, and P. P. Choi, Grain boundary segregation engineering in metallic alloys: A pathway to the design of interfaces, Curr. Opin. Solid State Mater. Sci. **18**, 253 (2014).

[4] K. A. Darling, M. A. Tschopp, B. K. VanLeeuwen, M. A. Atwater, and Z. K. Liu, Mitigating grain growth in binary nanocrystalline alloys through solute selection based on thermodynamic stability maps, Comput. Mater. Sci. **84**, 255 (2014).

[5] J. R. Trelewicz, and C. A. Schuh, Grain boundary segregation and thermodynamically stable binary nanocrystalline alloys, Phys. Rev. B **79**, 094112 (2009).

[6] C. C. Koch, R. O. Scattergood, K. A. Darling, and J. E. Semones, Stabilization of nanocrystalline grain sizes by solute additions, J. Mater. Sci. **43**, 7264 (2008).

[7] F. Abdeljawad, and S. M. Foiles, Stabilization of nanocrystalline alloys via grain boundary segregation: A diffuse interface model, Acta Mater. **101**, 159 (2015).

[8] A. Khalajhedayati, and T. J. Rupert, High-temperature stability and grain boundary complexion formation in a nanocrystalline Cu-Zr Alloy, JOM **67**, 2788 (2015).

[9] M. Kapoor, T. Kaub, K. A. Darling, B. L. Boyce, and G. B. Thompson, An atom probe study on Nb solute partitioning and nanocrystalline grain stabilization in mechanically alloyed Cu-Nb, Acta Mater. **126**, 564 (2017).

[10] C. A. Schuh, and K. Lu, Stability of nanocrystalline metals: The role of grain-boundary chemistry and structure, MRS Bull. **46**, 225 (2021).

[11] C. J. O'Brien, C. M. Barr, P. M. Price, K. Hattar, and S. M. Foiles, Grain boundary phase transformations in PtAu and relevance to thermal stabilization of bulk nanocrystalline metals, J. Mater. Sci. **53**, 2911 (2018).

[12] C. M. Barr, S. M. Foiles, M. Alkayyali, Y. Mahmood, P. M. Price, D. P. Adams, B. L. Boyce, F. Abdeljawad, and K. Hattar, The role of grain boundary character in solute segregation and thermal stability of nanocrystalline Pt–Au, Nanoscale **13**, 3552 (2021).

[13] P. Lu, F. Abdeljawad, M. Rodriguez, M. Chandross, D. P. Adams, B. L. Boyce, B. G. Clark, and N. Argibay, On the thermal stability and grain boundary segregation in nanocrystalline PtAu alloys, Materialia **6**, 100298 (2019).

[14] A. K. Barnett, O. Hussein, M. Alghalayini, A. Hinojos, J. E. Nathaniel II, D. L. Medlin, K. Hattar, B. L. Boyce, and F. Abdeljawad, Triple junction segregation dominates the stability of nanocrystalline alloys, Nano Lett. **24**, 9627 (2024).

[15] A. Gupta, X. Zhou, G. B. Thompson, and G. J. Tucker, Role of grain boundary character and its evolution on interfacial solute segregation behavior in nanocrystalline Ni-P, Acta Mater. **190**, 113 (2020).

[16] X. Zhou, A. Gupta, G. J. Tucker, and G. B. Thompson, Manipulation of solute partitioning mechanisms for nanocrystalline stability, Acta Mater. **208**, 116662 (2021).

[17] X. Zhou, X.-x. Yu, T. Kaub, R. L. Martens, and G. B. Thompson, Grain boundary specific segregation in nanocrystalline Fe(Cr), Sci. Rep. **6**, 34642 (2016).

[18] Z. Pan, and F. Sansoz, Heterogeneous solute segregation suppresses strain localization in nanocrystalline Ag-Ni alloys, Acta Mater. **200**, 91 (2020).

[19] Z. Pan, V. Borovikov, M. I. Mendelev, and F. Sansoz, Development of a semi-empirical potential for simulation of Ni solute segregation into grain boundaries in Ag, Model. Simul. Mater. Sci. Eng. **26**, 075004 (2018).

[20] E.-A. Picard, and F. Sansoz, Ni solute segregation and associated plastic deformation mechanisms into random FCC Ag, BCC Nb and HCP Zr polycrystals, Acta Mater. **240**, 118367 (2022).

[21] S. C. Pun, W. Wang, A. Khalajhedayati, J. D. Schuler, J. R. Trelewicz, and T. J. Rupert, Nanocrystalline Al-Mg with extreme strength due to grain boundary doping, Mater. Sci. Eng. A **696**, 400 (2017).

[22] S. V. Bobylev, N. A. Enikeev, A. G. Sheinerman, and R. Z. Valiev, Strength enhancement induced by grain boundary solute segregations in ultrafine-grained alloys, Int. J. Plast. **123**, 133 (2019).

[23] B. C. Hornbuckle, J. A. Smeltzer, S. Sharma, S. Nagar, C. J. Marvel, P. R. Cantwell, M. P. Harmer, K. Solanki, and K. A. Darling, A high-temperature nanostructured Cu-Ta-Li alloy with complexion-stabilized precipitates, Science **387**, 1413 (2025).

[24] K. A. Darling, M. Rajagopalan, M. Komarasamy, M. A. Bhatia, B. C. Hornbuckle, R. S. Mishra, and K. N. Solanki, Extreme creep resistance in a microstructurally stable nanocrystalline alloy, Nature (London) **537**, 378 (2016).

[25] C. E. Edwards, T. F. Babuska, J. F. Curry, F. W. DelRio, J. P. Killgore, B. L. Boyce, H.-M. Lien, M. T. Dugger, and F. Mangolini, Tunable amorphous carbon films formed on ultralow wear, Pt–Au alloys, Carbon **226**, 119220 (2024).

[26] R. Bueno Villoro, M. Wood, T. Luo, H. Bishara, L. Abdellaoui, D. Zavanelli, B. Gault, G. J. Snyder, C. Scheu, and S. Zhang, Fe segregation as a tool to enhance electrical conductivity of grain boundaries in Ti(Co,Fe)Sb half Heusler thermoelectrics, Acta Mater. **249**, 118816 (2023).

[27] D. P. Adams, R. Kothari, S. Addamane, M. Jain, K. Dorman, S. Desai, C. Sobczak, M. Kalaswad, N. Bianco, F. W. DelRio, J. O. Custer, M. A. Rodriguez, J. Boro, R. Dingreville, and B. L. Boyce, Guided combinatorial synthesis and automated characterization expedites the discovery of hard, electrically conductive Pt_xAu_{1-x} films, J. Vac. Sci. Technol. A **42**, 053411 (2024).

[28] J. K. Sunde, C. D. Marioara, S. Wenner, and R. Holmestad, On the microstructural origins of improvements in conductivity by heavy deformation and ageing of Al-Mg-Si alloy 6101, Mater. Charact. **176**, 111073 (2021).

[29] H. Song, and J. J. Hoyt, Barrier-free nucleation at grain-boundary triple junctions during solid-state phase transformations, Phys. Rev. Lett. **117**, 238001 (2016).

[30] F. Sansoz, and X. Ke, Hall–Petch strengthening limit through partially active segregation in nanocrystalline Ag-Cu alloys, Acta Mater. **225**, 117560 (2022).

[31] T. Nenninger, and F. Sansoz, Local atomic environment analysis of short and long-range solute-solute interactions in a symmetric tilt grain boundary, Scr. Mater. **222**, 115045 (2023).

[32] A. R. Denton, and N. W. Ashcroft, Vegard's law, Phys. Rev. A **43**, 3161 (1991).

[33] G. Kresse, and J. Furthmüller, Efficiency of *ab-initio* total energy calculations for metals and semiconductors using a plane-wave basis set, Comput. Mater. Sci. **6**, 15 (1996).

[34] J. P. Perdew, K. Burke, and M. Ernzerhof, Generalized gradient approximation made simple, Phys. Rev. Lett. **77**, 3865 (1996).

[35] W. Kohn, and L. J. Sham, Self-consistent equations including exchange and correlation effects, Phys. Rev. **140**, A1133 (1965).

[36] D. Bufford, H. Wang, and X. Zhang, High strength, epitaxial nanotwinned Ag films, Acta Mater. **59**, 93 (2011).

[37] J. Yeom, G. Lorenzin, C. Cancellieri, and J. Janczak-Rusch, Evaluation of residual stresses in Cu/Mo, Cu/Nb nanomultilayers with a strong fiber texture, Mater. Lett. **352**, 135074 (2023).

[38] G. Lorenzin, L. P. H. Jeurgens, and C. Cancellieri, Stress tuning in sputter-grown Cu and W films for Cu/W nanomultilayer design, J. Appl. Phys. **131**, 225304 (2022).

[39] G. Lorenzin, F. F. Klimashin, J. Yeom, Y. Hu, J. Michler, J. Janczak-Rusch, V. Turlo, and C. Cancellieri, Effect of residual stress and microstructure on mechanical properties of sputter-grown Cu/W nanomultilayers, APL Mater. **12**, 101109 (2024).

[40] V. I. Shapovalov, A. E. Komlev, A. S. Bondarenko, P. B. Baykov, and V. V. Karzin, Substrate heating and cooling during magnetron sputtering of copper target, Phys. Lett. A **380**, 882 (2016).

[41] T. Nenninger, and F. Sansoz, Solute clustering in polycrystals: Unveiling the interplay of grain boundary junction and long-range solute attraction effects, Acta Mater. **290**, 120946 (2025).

[42] F. Sansoz, and J. F. Molinari, Mechanical behavior of Σ tilt grain boundaries in nanoscale Cu and Al: A quasicontinuum study, Acta Mater. **53**, 1931 (2005).

[43] M. Wagih, and C. A. Schuh, Spectrum of grain boundary segregation energies in a polycrystal, Acta Mater. **181**, 228 (2019).

[44] T. P. Matson, and C. A. Schuh, Atomistic assessment of solute-solute interactions during grain boundary segregation, Nanomaterials **11**, 2360 (2021).

[45] S. Gohil, R. Banerjee, S. Bose, and P. Ayyub, Influence of synthesis conditions on the nanostructure of immiscible copper–silver alloy thin films, Scr. Mater. **58**, 842 (2008).

[46] F. Misják, P. B. Barna, and G. Radnóczi, Growth of nanocomposite in eutectic Cu–Ag films, Thin. Solid. Films **518**, 4247 (2010).

[47] D. Hamana, and L. Boumaza, Precipitation mechanism in Ag–8wt.% Cu alloy, J. Alloys Compd. **477**, 217 (2009).

[48] R. H. Nada, Precipitation kinetics in Ag–2wt% Cu and Ag–2wt% Cu–0.5wt% In alloys during transformation, Physica B **349**, 166 (2004).

[49] H. H. Wu, and D. R. Trinkle, Cu/Ag EAM potential optimized for heteroepitaxial diffusion from *ab initio* data, Comput. Mater. Sci. **47**, 577 (2009).

[50] P. L. Williams, Y. Mishin, and J. C. Hamilton, An embedded-atom potential for the Cu–Ag system, Modell. Simul. Mater. Sci. Eng. **14**, 817 (2006).

[51] X. W. Zhou, R. A. Johnson, and H. N. G. Wadley, Misfit-energy-increasing dislocations in vapor-deposited CoFe/NiFe multilayers, Phys. Rev. B **69**, 144113 (2004).

[52] T. Frolov, M. Asta, and Y. Mishin, Segregation-induced phase transformations in grain boundaries, Phys. Rev. B **92**, 020103(R) (2015).

[53] D. Hamana, M. Hachouf, L. Boumaza, and Z. E. A. Biskri, Precipitation kinetics and mechanism in Cu-7 wt% Ag alloy, Mater. Sci. Appl. **2**, 899 (2011).

[54] R. K. Koju, and Y. Mishin, Relationship between grain boundary segregation and grain boundary diffusion in Cu-Ag alloys, Phys. Rev. Mater. **4**, 073403 (2020).

[55] X. Shuai, Z. J. Wang, H. Mao, S. Tang, Y. Kong, and Y. Du, Atomic-scale study of compositional and structural evolution of early-stage grain boundary precipitation in Al–Cu alloys through phase-field crystal simulation, J. Mater. Sci. **56**, 12700 (2021).

[56] P. Nikitin, M. Guinel de France, and F. Sansoz, The physical origin of heterogeneous solute clustering and nanoprecipitation at grain boundaries in ultrafine-grained immiscible alloys, Scr. Mater. **270**, 116939 (2026).